photonics

Communication

High-Linearity Dual-Parallel Mach–Zehnder Modulators in Thin-Film Lithium Niobate

Tao Yang, Lutong Cai *, Zhanhua Huang and Lin Zhang *

State Key Laboratory of Precision Measurement Technology and Instruments, Key Laboratory of Opto-Electronic Information Technology of Ministry of Education, Tianjin Key Laboratory of Integrated Opto-Electronics Technologies and Devices, School of Precision Instruments and Opto-Electronics Engineering, Tianjin University, Tianjin 300072, China; yangtao1999@tju.edu.cn (T.Y.); zhanhua@tju.edu.cn (Z.H.)

* Correspondence: lutong_cai@tju.edu.cn (L.C.); lin_zhang@tju.edu.cn (L.Z.)

Abstract: Microwave photonic (MWP) systems are inseparable from conversions of microwave electrical signals into optical signals, and their performances highly depend on the linearity of electro-optic modulators. Thin-film lithium niobate (TFLN) is expected to be an ideal platform for future microwave photonic systems due to its compact size, low optical loss, linear electro-optic effect, and high bandwidth. In this paper, we propose a TFLN modulator with a low voltage–length product ($V_{\pi}L$) of 1.97 V·cm and an ultra-high-linearity carrier-to-distortion ratio (CDR) of 112.33 dB, using a dual-parallel Mach–Zehnder interferometer configuration. It provides an effective approach to fully suppress the third-order intermodulation distortions (IMD3), leading to 76 dB improvement over a single Mach–Zehnder modulator (MZM) in TFLN. The proposed TFLN modulator would enable a wide variety of applications in integrated MWP systems with large-scale integration, low power consumption, low optical loss, and high bandwidth.

Keywords: linearity; Mach–Zehnder modulators; thin-film lithium niobate; integrated microwave photonic systems

check for updates

Citation: Yang, T.; Cai, L.; Huang, Z.; Zhang, L. High-Linearity Dual-Parallel Mach–Zehnder Modulators in Thin-Film Lithium Niobate. *Photonics* **2024**, *11*, 987. https://doi.org/10.3390/photonics11100987

Received: 18 September 2024
Revised: 13 October 2024
Accepted: 18 October 2024
Published: 20 October 2024

1. Introduction

For decades, lithium niobate ($LiNbO_3$, LN) has been one of the most versatile and attractive multifunctional optical materials, owing to its wide transparent windows, low intrinsic absorption, and exceptional electro-, nonlinear-, and acousto-optic properties [1]. Conventional LN photonic devices are based on low-index-contrast waveguides commonly formed by titanium in-diffusion [2] and proton exchange process [3]. However, these conventional LN optical waveguides are relatively bulky compared with modern integrated platforms, such as silicon photonics, which impedes scalability and leads to high power consumption for electro-optic (EO) devices. The high-quality TFLN fabricated by ion slicing and wafer bonding enables high-index-contrast and low-loss wave-guides with strong optical confinements [4–7]. In recent years, a variety of integrated photonic devices have been developed on the TFLN platform with higher performance [8–13] compared with traditional bulk LN devices.

MWP systems achieve the generation, transmission, and processing of microwave signals in the optical domain by virtue of the high bandwidth, low transmission loss, and anti-electromagnetic interference of optical components. A variety of key components of MWP systems have been realized such as microwave photonic phased arrays [14], ultra-wideband waveform generators [15–18], photonic analog-to-digital converter [19], photonic microwave filters [20,21], and so on. Moreover, integrated microwave photonic systems with small size, low power consumption, low cost, and high stability can be further realized by integrating discrete optoelectronic devices on a chip. EO modulators stand as one of the most important components in the MWP link, and TFLN modulators are attractive for developing integrated MWP systems due to their ultra-high bandwidths beyond 100 GHz, CMOS-compatible drive voltages, and low optical losses [8,9,22,23].

In MWP links, the nonlinearities of EO modulators can introduce additional higher-order harmonics and intermodulation distortions to the signals [24,25]. Modulation linearity is often quantified as spurious free dynamic range (SFDR) [25] or CDR [26]. As LN possesses linear electric-optic effect (also called Pockels effect), linearizing a LN modulator is much simpler and more robust than linearizing a silicon (Si) or indium phosphide (InP) modulator [27], which involves intrinsically nonlinear modulation mechanisms [28,29]. Therefore, one just needs to compensate for the nonlinear transfer function of a simple Mach–Zehnder interferometer (MZI) in LN. In order to linearize MZM, a lot of methods have been developed in both the electrical domain and the optical domain. Traditional linearization methods in the electrical domain require relatively complex equipment for electronic control [30,31]. Linearization strategies in the optical domain generally include dual-polarization control [32], microring-assisted MZI (RAMZI) [33], and dual-series [34] and dual-parallel [35] MZMs. These methods directly eliminate IMD3 in modulators by regulating the characteristics of light, greatly improving the linearity without affecting electrical signals and requiring additional nonlinearity compensation equipment. Traditional high-linearity LN modulators based on dual-series and dual-parallel MZMs have been demonstrated with an ultra-high SFDR of 132 dB·Hz$^{2/3}$ [34] and 123.4 dB·Hz$^{2/3}$ [35], respectively. On the TFLN platform, RAMZI with a high SFDR of 120.04 dB·Hz$^{4/5}$ has been demonstrated [33]. However, the EO bandwidth of RAMZI is constrained by the photon lifetime of a ring resonator, so the amplitude of the first-order harmonic (FH) component and CDR value drop at high radio frequency (RF). The operating wavelength bandwidth is also narrow at the Fano resonance [33]. The dual-series and dual-parallel MZMs are relatively simple and effective to achieve high linearity, EO bandwidth, and optical bandwidth, but neither has been demonstrated on the TFLN platform.

In this paper, we apply the dual-parallel MZM configuration to TFLN modulators to achieve high linearity. Modulation efficiency is optimized first to achieve a low $V_\pi L$ of 1.97 V·cm. Furthermore, simulation results show that IMD3 can be completely suppressed by controlling splitting ratios of optical and RF signals. Meanwhile, the dual-parallel MZM has a CDR of 112.33 dB, which is 76 dB higher than that of a single MZM with the same modulation efficiency.

2. Device and Principle

2.1. Device Configuration

Figure 1 shows our proposed dual-parallel MZM on TFLN. The third-order nonlinearities of two MZMs can cancel each other out by controlling splitting ratios of optical and RF signals [35]. To maximize modulation efficiency, the proposed structure is based on a 600 nm thick x-cut TFLN, sitting on top of a 4.7 µm thick SiO_2 layer. The input light propagates along the y-axis of LN and is equally split into two arms by a 1 × 2 multimode interferometer (MMI) and then combined by a 2 × 2 MMI. A direct current (DC) voltage induces a phase difference φ_0 between the two arms to tune the ratio of optical powers feeding to the two parallel MZMs. The two parallel MZMs both have ground–signal–ground (GSG) electrode configuration and share a common ground electrode to reduce footprint. The normalized optical power feeding to the sub-MZM can be calculated as $\beta = (1 + \sin\varphi_0)/2$ [27]. The RF signal, v_{rf}, is split into two sub-MZMs with a power ratio of $\gamma : (1 - \gamma)$. The two RF signals are combined with their respective DC bias voltages, V_{DC}, by bias-tees before driving the two MZMs. Therefore, MZM_1 and MZM_2 are driven by different RF powers of $\sqrt{\gamma}v_{\mathrm{rf}}$ and $\sqrt{1-\gamma}v_{\mathrm{rf}}$, respectively. The DC bias voltages are denoted as V_{DC1} and V_{DC2}. The driving signal induces the phase difference $\Delta\theta(V)$. When both MZMs are biased at the quadrature points to maximize the modulation efficiency, i.e.,

$\Delta\theta(V_{\mathrm{DC1}}) = \pi/2$, and $\Delta\theta(V_{\mathrm{DC2}}) = -\pi/2$, the output optical power of this device is given by [27]:

$$\begin{aligned} I_{\mathrm{out}} &= \frac{|E_{\mathrm{in}}|^2}{8}\begin{bmatrix} 2-(1+\sin\varphi_0)\sin\left[\Delta\theta\left(\sqrt{\gamma}v_{\mathrm{rf}}, V_{\mathrm{DC}}\right)\right] \\ +(1-\sin\varphi_0)\sin\left[\Delta\theta\left(\sqrt{1-\gamma}v_{\mathrm{rf}}, V_{\mathrm{DC}}\right)\right] \end{bmatrix} \\ &= \frac{|E_{\mathrm{in}}|^2}{8}\begin{bmatrix} 2-(1+\sin\varphi_0)\left(\Delta\theta\left(\sqrt{\gamma}v_{\mathrm{rf}}, V_{\mathrm{DC}}\right)-\frac{1}{3!}\Delta\theta^3\left(\sqrt{\gamma}v_{\mathrm{rf}}, V_{\mathrm{DC}}\right)\right) \\ +(1-\sin\varphi_0)\left(\Delta\theta\left(\sqrt{1-\gamma}v_{\mathrm{rf}}, V_{\mathrm{DC}}\right)-\frac{1}{3!}\Delta\theta^3\left(\sqrt{1-\gamma}v_{\mathrm{rf}}, V_{\mathrm{DC}}\right)\right) \end{bmatrix} \end{aligned} \tag{1}$$

Due to the linear EO effect of LN, $\Delta\theta(V)$ can be simply written as

$$\Delta\theta(V) = \frac{2\pi}{\lambda}L\Delta n_{eff}(V) = \frac{2\pi}{\lambda}LkV \tag{2}$$

where L is the length of EO interaction, $\Delta n_{eff}(V)$ is the change in the effective refractive index, and k is a constant related to material properties and waveguide geometries.

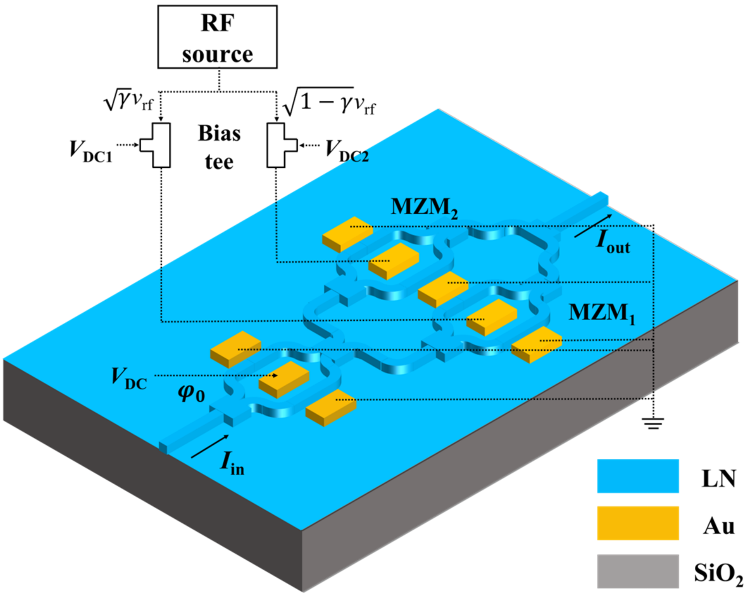

Figure 1. Schematic of the dual-parallel MZM in TFLN.

2.2. Nonlinearity Evaluation

The nonlinearity of a modulator is typically probed by a technique known as two-tone test, which utilizes a pair of two closely spaced tones (f_1 and f_2) to drive the modulator. The IMD3 components are at frequencies of $2f_1 - f_2$ and $2f_2 - f_1$. The FH and IMD3 components of the modulated optical field can be derived by performing Taylor expansion at the corresponding bias point [27]:

$$A_{\mathrm{FH}}\cos(\omega t) = \left(v_0\left[\frac{dI_{\mathrm{out}}}{dv}\right] + \frac{9}{4}v_0^3\left[\frac{1}{3!}\frac{d^3I_{\mathrm{out}}}{dv^3}\right] + \frac{25}{4}v_0^5\left[\frac{1}{5!}\frac{d^5I_{\mathrm{out}}}{dv^5}\right]\right)_{v=V_{\mathrm{DC}}}\cos(\omega t) \tag{3}$$

$$A_{\mathrm{IMD3}}\cos((2\omega_1-\omega_2)t) = \left(\frac{3}{4}v_0^3\left[\frac{1}{3!}\frac{d^3I_{\mathrm{out}}}{dv^3}\right] + \frac{25}{8}v_0^5\left[\frac{1}{5!}\frac{d^5I_{\mathrm{out}}}{dv^5}\right]\right)_{v=V_{\mathrm{DC}}}\cos((2\omega_1-\omega_2)t) \tag{4}$$

where A_{FH} and A_{IMD3} represent the amplitudes of the FH and IMD3 components, respectively, and v_0 denotes the amplitude of the RF signal.

By plugging Equations (3) and (4) into Equation (1), we obtain the amplitude of the FH and IMD3 components of the dual-parallel MZM.

$$A_{\mathrm{FH}} = \tfrac{1}{8}v_0\tfrac{2\pi}{\lambda}Lk\left[-(1+\sin\varphi_0)\sqrt{\gamma}+(1-\sin\varphi_0)\sqrt{1-\gamma}\right]+ \\ \tfrac{3}{64}v_0^3(\tfrac{2\pi}{\lambda}Lk)^3\left[(1+\sin\varphi_0)(\sqrt{\gamma})^3-(1-\sin\varphi_0)(\sqrt{1-\gamma})^3\right] \tag{5}$$

$$A_{\mathrm{IMD3}} = \frac{3}{32}v_0^3(\frac{2\pi}{\lambda}Lk)^3\left[-(1+\sin\varphi_0)(\sqrt{\gamma})^3+(1-\sin\varphi_0)(\sqrt{1-\gamma})^3\right] \tag{6}$$

The CDR is defined as

$$CDR = \frac{P_{\mathrm{IMD3}}}{P_{\mathrm{FH}}} = \frac{\frac{R_D}{2}(P_L\eta A_{\mathrm{IMD3}})^2}{\frac{R_D}{2}(P_L\eta A_{\mathrm{FH}})^2} \tag{7}$$

where P_{IMD3} and P_{FH} represent RF powers of IMD3 and FH components in the output of the receiver. R_D, η, and P_L denote the detector load, detector responsivity, and laser power, respectively. Their typical values, listed in Table 1, are used to calculate the nonlinear distortion.

Table 1. Link parameters used to evaluate CDR.

Symbol	Quantity	Value
R_D	Detector Load	50 Ω
η	Detector Responsivity	0.7 A/W
P_L	Laser Power	0.01 W

3. Optimization of Modulation Efficiency and Linearity

3.1. Optimization of Modulation Efficiency

Figure 2a shows the cross-section of the phase shifter area in the dual-parallel MZM. The TFLN waveguide has an etching depth, h, of 300 nm and a sidewall angle, θ, of 70 degrees. The 300 nm etching depth can achieve both low bending loss and high modulation efficiency. Figure 2b,c show the simulated electric field (1 V is applied to the electrodes) and optical TE_{00} mode, respectively. The electric field changes the refractive index of LN, thus changing the effective refractive index of the waveguide mode, which can be expressed as [36]

$$\Delta n_{eff} = -\frac{n_e^3 r_{33} V}{2}\cdot\Gamma \tag{8}$$

$$\Gamma \equiv \frac{\iint_{S_{\mathrm{LN}}}\frac{E_{ele}(\mathrm{x,z})}{\mathrm{V}}\cdot|E_o(\mathrm{x,z})|^2\mathrm{dxdz}}{\int_{-\infty}^{+\infty}\int_{-\infty}^{+\infty}|E_o(\mathrm{x,z})|^2\mathrm{dxdz}} \tag{9}$$

where n_e is the extraordinary index of LN, r_{33} is the electro-optical coefficient of LN, $E_o(\mathrm{x,z})$ is the electric field of the optical TE_{00} mode, and $E_{ele}(\mathrm{x,z})$ is the electric field of the RF signal along the z-axis. Γ represents the overlap between optical and electrical fields. Thus, the k in Equation (2) can be calculated by

$$k = -\frac{n_e^3 r_{33}}{2}\cdot\Gamma \tag{10}$$

and the $\mathrm{V}_\pi\mathrm{L}$, which quantifies modulation efficiency, can be expressed as [36]

$$V_\pi L = \frac{\lambda}{2{n_e}^3 r_{33}\Gamma} \tag{11}$$

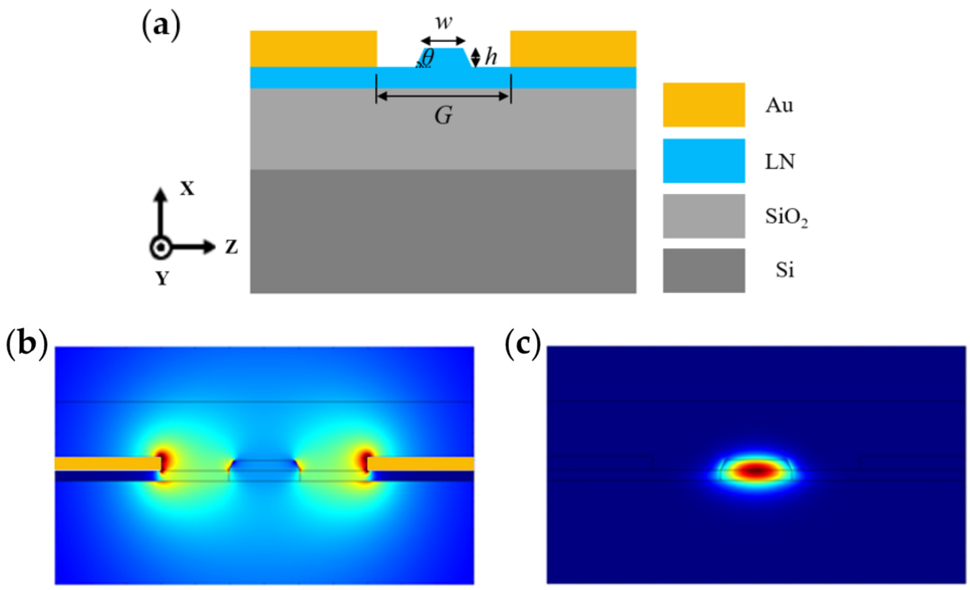

Figure 2. (**a**) The cross-section of the phase shifter area. (**b**) RF electric field distribution and (**c**) electric field of the optical TE$_{00}$ mode.

Figure 3 shows the dependence of V$_\pi$L on waveguide width and the gap between the electrodes. It can be seen that V$_\pi$L would be lower with a larger top width, w, of the ridge waveguide and a narrower gap, G, between the electrodes. Considering the optical loss caused by electrode absorption, we highlight the relation between w and G (black line) under the condition that the optical loss is 0.1 dB/cm, and find that the lowest V$_\pi$L is 1.97 V·cm when w and G are 1.3 µm and 4.6 µm, respectively. The optical loss of 0.1 dB/cm is almost negligible and thus satisfies the approximation of linearity calculation.

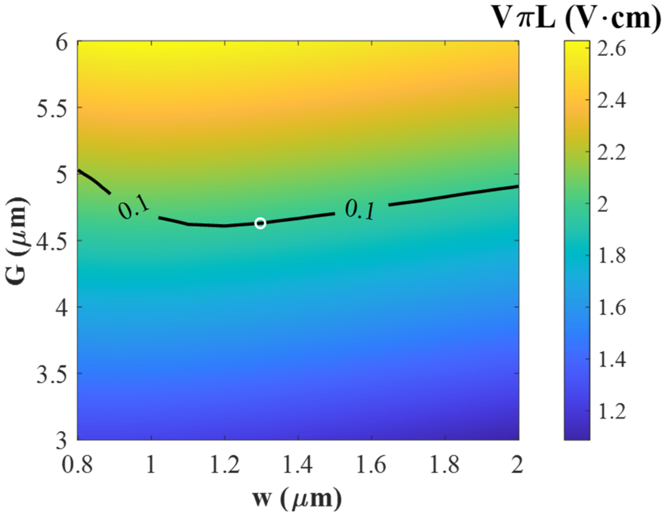

Figure 3. Calculated V$_\pi$L and optical loss induced by metal absorption as a function of waveguide width and electrode gap. The white circle indicates the positions for the lowest V$_\pi$L on the contour line of 0.1 dB/cm loss.

3.2. Optimization of Modulation Linearity

Using the optimized geometry of the phase shifter, the value of k can be calculated according to Equation (2). Then, we can quantitate modulation linearity. Figure 4a,b show the powers of FH and IMD3 components as a function of optical power splitting ratio, β, and RF power splitting ratio, γ, respectively. The parameters used in calculation are as follows: λ= 1550 nm; L = 5 mm; and v_0 = 1 V. Because two sub-MZMs operate at the quadrature bias points of $\pi/2$ and $-\pi/2$, the DC bias voltages are V_{DC1} = 1.97 V and

V_{DC2} = −1.97 V according to $V_{\pi}L$ = 1.97 V·cm. Based on the results shown in Figure 4a,b, the CDR defined in Equation (7) is plotted as a function of γ and β in Figure 4c. It can be seen that the IMD3 component can be completely eliminated in Figure 4b, which leads to the high CDR in Fig-ure 4c. However, the FH component can be very weak in Figure 4a, which produces the low CDR in Figure 4c. Figure 4d illustrates two relationships between γ and β, corresponding to the conditions that the amplitudes of the FH and IMD3 components are 0. The values of γ and β should be chosen on the curve of P_{IMD3} = 0 and away from the area of P_{FH} approaching 0. Maximum CDRs are marked as white circles in Figure 4c.

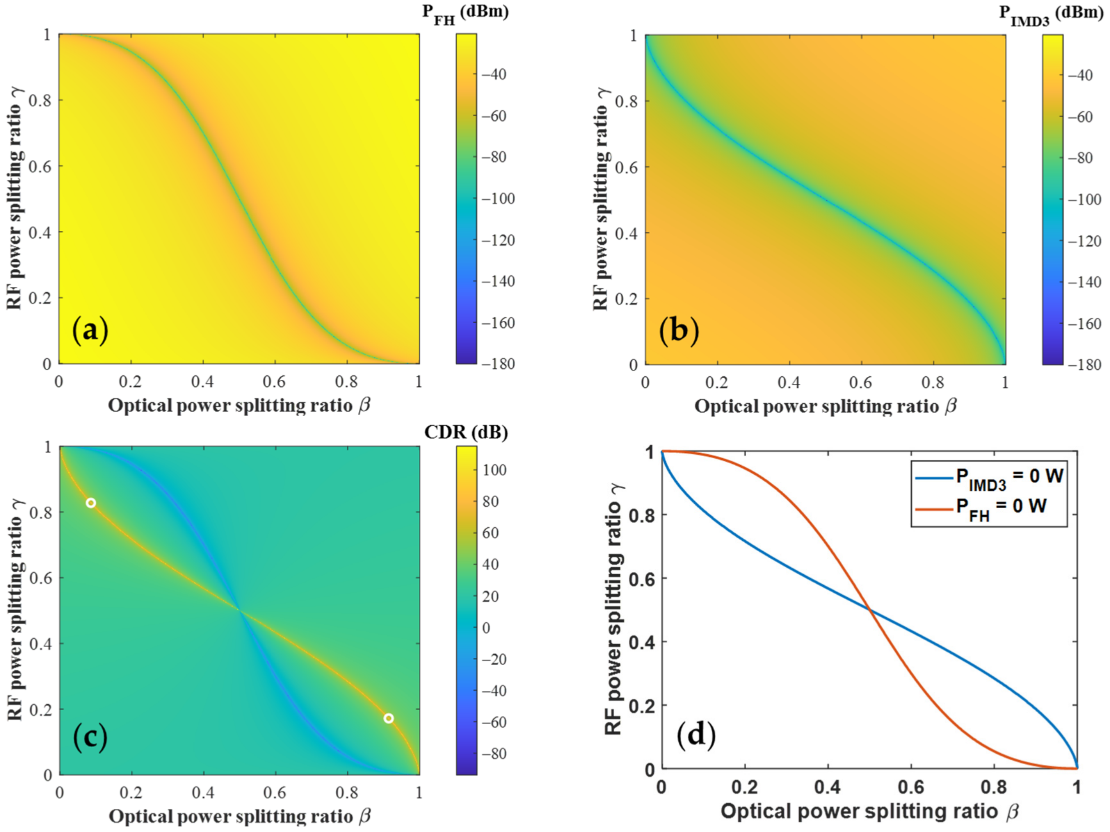

Figure 4. Calculated (**a**) power of the FH component, (**b**) power of the IMD3 component, and (**c**) CDR at different power splitting ratios. (**d**) The relationships between RF power splitting ratio and optical power splitting ratio when the powers of the FH and IMD3 components are 0.

The relationship between the FH power and γ when the IMD3 component is fully eliminated (blue line in Figure 4d) is plotted in Figure 5a. It can be observed that when γ = 0.172 and β = 0.914, the IMD3 component is fully eliminated while the FH power and CDR reach the maximum of −30.76 dBm and 112.33 dB, respectively. When β is 0.914, φ_0 is 0.976, and the corresponding DC bias voltage is 1.22 V. This point thus can be regarded as the optimal operation point to obtain the highest modulation linearity. The curve in Figure 5a is symmetric with respect to the vertical line of γ = 0.5 because of the same structure of two MZMs. Then, we calculate the FH power for other phase shifter lengths by taking the same procedure of obtaining the optimum combination of γ and β as mentioned above. The result is presented in Figure 5b. It can be seen that the optimum values of γ and β are insusceptible to the length of the phase shifter. On the other hand, the RF power of the FH components increases as the phase shifter becomes longer. Note that the large modulation length can also lead to low half-wave voltage but low EO bandwidth [22]. The length near 5 mm thus represents the optimal modulation length of the dual-parallel MZM.

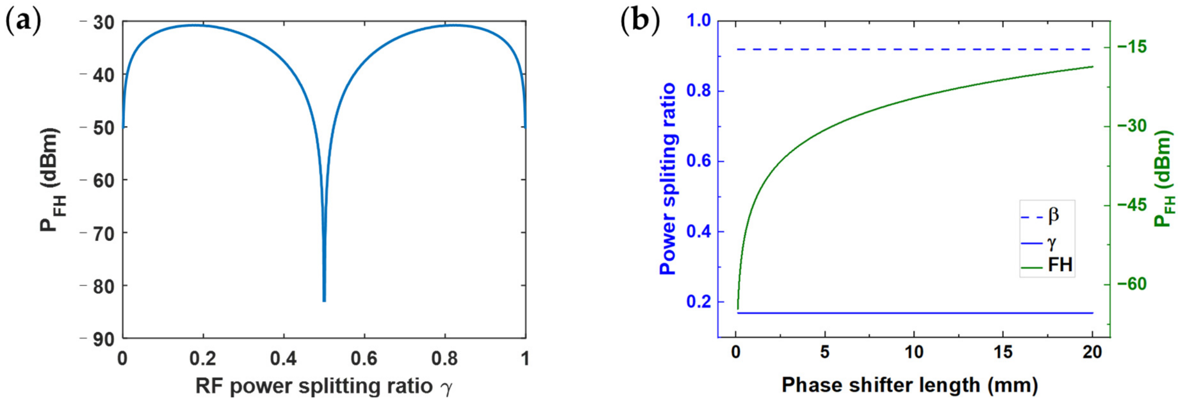

Figure 5. (**a**) The relationship between the power of the FH component and the RF power splitting ratio under the condition of P_{IMD3} = 0. (**b**) The power splitting ratios (both γ and β) and the FH power at different phase shifter lengths.

To linearize the modulation of the dual-parallel MZM, γ and β should be precisely set at the optimum values. Considering the difficulty in controlling γ and β exactly at their optimal values in practice, the power of the FH component, the power of the IMD3 component, and the CDR of the optimized dual-parallel MZM are calculated, while γ and β deviate from their ideal values, as shown in Figure 6a,c. The CDR of the dual-parallel MZM falls to ~30 dB, when the variations in γ and β are within ±10%.

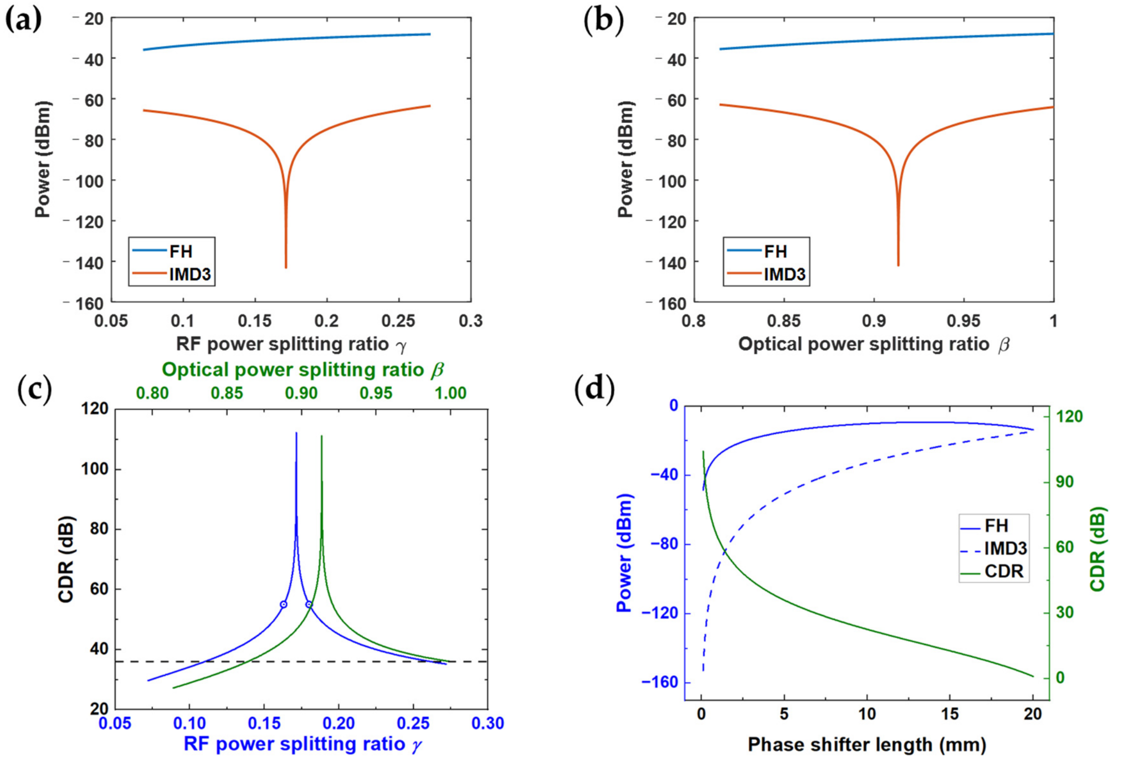

Figure 6. Variations in the powers of FH and IMD3 components of the dual-parallel MZM at a different (**a**) RF power splitting ratio and (**b**) optical power splitting ratio near their optimal values. (**c**) Degradations of CDR as the power splitting ratios (both γ and β) deviate from their ideal values. (**d**) Performance of the modulation linearity of the single MZM at different phase shifter lengths.

In the experimental system, γ can be controlled by an electric coupler and an adjustable attenuator [37]. When the attenuator has a typical precision of 0.2 dB in commercially available components, the CDR falls to 55 dB for the worst deviation, which is marked as the dots in Figure 6c. β is controlled by a stabilized DC voltage supply which has a common precision of 0.1%, and thus its influence on the CDR can be ignored.

Furthermore, we calculate the powers of the FH and IMD3 components of a single MZM, which has the same dimension as one MZM of the dual-parallel MZM, by taking the derivatives of its output light, as shown in Figure 6d. The IMD3 component cannot be suppressed, so the CDR in Figure 6d is much lower than that of the dual-parallel MZM. The CDR is 36 dB for a 5 mm long phase shifter in the single MZM in Figure 6d, which is also marked as a black dash-dotted line in Figure 6c for comparison. Therefore, the dual-parallel MZM has higher modulation linearity than the single MZM by at least 20 dB, even taking into account the variation in the splitting power in practice.

4. Conclusions

In summary, we demonstrate the design and optimization of a high-linearity dual-parallel MZM in TFLN platform. The modulator achieves a high CDR of 112 dB by optimizing the power splitting ratios of RF and optical signals, which is improved by 76 dB compared with the single MZM. The high linearity is attributed to the compensation of the IMD3 components induced by two parallel MZMs in this device. Consequently, the proposed device architecture substantially enhances the linearity of TFLN MZMs, holding great promise for applications in integrated MWP systems. In the future, we will fabricate the device proposed in this work and compare its performance with that of the single MZM.

Author Contributions: T.Y.: conceptualization, methodology, software, investigation, formal analysis, and writing—original draft; Z.H.: conceptualization, resources, and supervision; L.C.: conceptualization, resources, supervision, and writing—review and editing; L.Z.: conceptualization, resources, supervision, and writing—review and editing. All authors have read and agreed to the published version of the manuscript.

Funding: This research received no external funding.

Institutional Review Board Statement: Not applicable.

Informed Consent Statement: Not applicable.

Data Availability Statement: Data are contained within the article.

Conflicts of Interest: The authors declare no conflicts of interest.

References

1. Zhu, D.; Shao, L.; Yu, M.; Cheng, R.; Desiatov, B.; Xin, C.J.; Lončar, M. Integrated photonics on thin-film lithium niobate. *Adv. Opt. Photonics* **2021**, *13*, 242–352. [CrossRef]
2. Schmidt, R.V.; Kaminow, I.P. Metal-diffused optical waveguides in $LiNbO_3$. *Appl. Phys. Lett.* **1974**, *25*, 458–460. [CrossRef]
3. Jackel, J.L.; Rice, C.E.; Veselka, J.J. Proton exchange for high-index waveguides in $LiNbO_3$. *Appl. Phys. Lett.* **1982**, *41*, 607–608. [CrossRef]
4. Wu, R.; Wang, M.; Xu, J.; Qi, J.; Chu, W.; Fang, Z.; Cheng, Y. Long low-loss-litium niobate on insulator waveguides with sub-nanometer surface roughness. *Nanomaterials* **2018**, *8*, 910. [CrossRef]
5. Wolf, R.; Breunig, I.; Zappe, H.; Buse, K. Scattering-loss reduction of ridge waveguides by sidewall polishing. *Opt. Express* **2018**, *26*, 19815–19820. [CrossRef] [PubMed]
6. Ding, T.; Zheng, Y.; Chen, X. On-chip solc-type polarization control and wavelength filtering utilizing periodically poled lithium niobate on insulator ridge waveguide. *J. Light. Technol.* **2019**, *37*, 1296–1300. [CrossRef]
7. Zhang, M. Monolithic ultra-high-Q lithium niobate microring resonator. *Optica* **2017**, *4*, 1536–1537. [CrossRef]
8. Wang, C.; Zhang, M.; Chen, X.; Bertrand, M.; Shams-Ansari, A.; Chandrasekhar, S.; Lončar, M. Integrated lithium niobate electro-optic modulators operating at CMOS-compatible voltages. *Nature* **2018**, *562*, 101–104. [CrossRef]
9. He, M.; Xu, M.; Ren, Y.; Jian, J.; Ruan, Z.; Xu, Y.; Cai, X. High-performance hybrid silicon and lithium niobate Mach–Zehnder modulators for 100 Gbit s−1 and beyond. *Nat. Photonics* **2019**, *13*, 359–364. [CrossRef]
10. Guo, Q.; Gutierrez, B.K.; Sekine, R.; Gray, R.M.; Williams, J.A.; Ledezma, L.; Marandi, A. Ultrafast mode-locked laser in nanophotonic lithium niobate. *Science* **2023**, *382*, 708–713. [CrossRef]
11. Chen, J.Y.; Ma, Z.H.; Sua, Y.M.; Li, Z.; Tang, C.; Huang, Y.P. Ultra-efficient frequency conversion in quasi-phase-matched lithium niobate microrings. *Optica* **2019**, *6*, 1244–1245. [CrossRef]

12. Zhang, M.; Buscaino, B.; Wang, C.; Shams-Ansari, A.; Reimer, C.; Zhu, R.; Lončar, M. Broadband electro-optic frequency comb generation in a lithium niobate microring resonator. *Nature* **2019**, *568*, 373–377. [CrossRef]
13. Zhao, J.; Ma, C.; Rüsing, M.; Mookherjea, S. High quality entangled photon pair generation in periodically poled thin-film lithium niobate waveguides. *Phys. Rev. Lett.* **2020**, *124*, 163603. [CrossRef] [PubMed]
14. Wu, P.; Tang, S.; Raible, D.E. A prototype high-speed optically-steered X-band phased array antenna. *Opt. Express* **2013**, *21*, 32599–32604. [CrossRef] [PubMed]
15. Mirshafiei, M.; LaRochelle, S.; Rusch, L.A. Optical UWB waveform generation using a micro-ring resonator. *IEEE Photonics Technol. Lett.* **2012**, *24*, 1316–1318. [CrossRef]
16. Zhou, G.; Zhou, L.; Lu, L.; Guo, Y.; Chen, J. Phase-coded microwave signal generation based on a segmented silicon Mach–Zehnder modulator. *IEEE J. Sel. Top. Quantum Electron.* **2019**, *26*, 3500108. [CrossRef]
17. Zhong, Y.; Zhou, L.; Zhou, Y.; Xia, Y.; Liu, S.; Lu, L.; Wang, X. Microwave frequency upconversion employing a coupling-modulated ring resonator. *Photonics Res.* **2017**, *5*, 689–694. [CrossRef]
18. Long, Y.; Zhou, L.; Wang, J. Photonic-assisted microwave signal multiplication and modulation using a silicon Mach–Zehnder modulator. *Sci. Rep.* **2016**, *6*, 20215. [CrossRef]
19. Valley, G.C. Photonic analog-to-digital converters. *Opt. Express* **2007**, *15*, 1955–1982. [CrossRef]
20. Gutierrez, A.M.; Sanchis, P.; Brimont, A.; Thomson, D.J.; Gardes, F.Y.; Reed, G.T.; Vidal, B. A photonic microwave filter based on an asymmetric silicon Mach-Zehnder modulator. *IEEE Photonics J.* **2013**, *5*, 5501006. [CrossRef]
21. Sun, Q.; Zhou, L.; Lu, L.; Zhou, G.; Chen, J. Reconfigurable high-resolution microwave photonic filter based on dual-ring-assisted MZIs on the Si_3N_4 platform. *IEEE Photonics J.* **2018**, *10*, 1–12. [CrossRef]
22. Kharel, P.; Reimer, C.; Luke, K.; He, L.; Zhang, M. Breaking voltage–bandwidth limits in integrated lithium niobate modulators using micro-structured electrodes. *Optica* **2021**, *8*, 357–363. [CrossRef]
23. Xu, M.; Zhu, Y.; Pittalà, F.; Tang, J.; He, M.; Ng, W.C.; Cai, X. Dual-polarization thin-film lithium niobate in-phase quadrature modulators for terabit-per-second transmission. *Optica* **2022**, *9*, 61–62. [CrossRef]
24. Feng, H.; Ge, T.; Guo, X.; Wang, B.; Zhang, Y.; Chen, Z.; Wang, C. Integrated lithium niobate microwave photonic processing engine. *Nature* **2024**, *627*, 80–87. [CrossRef] [PubMed]
25. Marpaung, D.; Roeloffzen, C.; Heideman, R.; Leinse, A.; Sales, S.; Capmany, J. Integrated microwave photonics. *Laser Photonics Rev.* **2013**, *7*, 506–538. [CrossRef]
26. Song, M.; Zhang, L.; Beausoleil, R.G.; Willner, A.E. Nonlinear distortion in a silicon microring-based electro-optic modulator for analog optical links. *IEEE J. Sel. Top. Quantum Electron.* **2009**, *16*, 185–191. [CrossRef]
27. Zhang, Q.; Yu, H.; Jin, H.; Qi, T.; Li, Y.; Yang, J.; Jiang, X. Linearity comparison of silicon carrier-depletion-based single, dual-parallel, and dual-series Mach–Zehnder modulators. *J. Light. Technol.* **2018**, *36*, 3318–3331. [CrossRef]
28. Manolatou, C.; Lipson, M. All-optical silicon modulators based on carrier injection by two-photon absorption. *J. Light. Technol.* **2006**, *24*, 1433. [CrossRef]
29. Miller, D.A.; Chemla, D.S.; Damen, T.C.; Gossard, A.C.; Wiegmann, W.; Wood, T.H.; Burrus, C.A. Band-edge electroabsorption in quantum well structures: The quantum-confined Stark effect. *Phys. Rev. Lett.* **1984**, *53*, 2173. [CrossRef]
30. Childs, R.B.; O'Byrne, V.A. Multichannel AM video transmission using a high-power Nd: YAG laser and linearized external modulator. *IEEE J. Sel. Areas Commun.* **1990**, *8*, 1369–1376. [CrossRef]
31. Clark, T.R.; Currie, M.; Matthews, P.J. Digitally linearized wide-band photonic link. *J. Light. Technol.* **2001**, *19*, 172–179. [CrossRef]
32. Johnson, L.M.; Roussell, H.V. Reduction of intermodulation distortion in interferometric optical modulators. *Opt. Lett.* **1988**, *13*, 928–930. [CrossRef] [PubMed]
33. Feng, H.; Zhang, K.; Sun, W.; Ren, Y.; Zhang, Y.; Zhang, W.; Wang, C. Ultra-high-linearity integrated lithium niobate electro-optic modulators. *Photonics Res.* **2022**, *10*, 2366–2373. [CrossRef]
34. Betts, G.E. Linearized modulator for suboctave-bandpass optical analog links. *IEEE Trans. Microw. Theory Tech.* **1994**, *42*, 2642–2649. [CrossRef]
35. Korotky, S.K.; De Ridder, R.M. Dual parallel modulation schemes for low-distortion analog optical transmission. *IEEE J. Sel. Areas Commun.* **1990**, *8*, 1377–1381. [CrossRef]
36. Liu, Y.; Li, H.; Liu, J.; Tan, S.; Lu, Q.; Guo, W. Low $V\pi$ thin-film lithium niobate modulator fabricated with photolithography. *Opt. Express* **2021**, *29*, 6320–6329. [CrossRef]
37. Wang, R.; Gao, Y.; Wang, W.; Zhang, J.; Tan, Q.; Fan, Y. Suppression of third-order intermodulation distortion in analog photonic link based on an integrated polarization division multiplexing Mach–Zehnder modulator. *Opt. Commun.* **2020**, *475*, 126253. [CrossRef]